IEEE Robotics and Automation Letters (RA-L) paper, presented at ICRA 2024, Yokohama, Japan. Cite as RA-L paper.

A Convex Formulation of Frictional Contact between Rigid and Deformable Bodies

Xuchen Han, Joseph Masterjohn, Alejandro Castro

***Abstract*—We present a novel convex formulation that models rigid and deformable bodies coupled through frictional contact. The formulation incorporates a new corotational material model with positive semi-definite Hessian, which allows us to extend our previous work on the convex formulation of compliant contact to model large body deformations. We rigorously characterize our approximations and present implementation details. With proven global convergence, effective warm-start, the ability to take large time steps, and specialized sparse algebra, our method runs robustly at interactive rates. We provide validation results and performance metrics on challenging simulations relevant to robotics applications. Our method is made available in the open-source robotics toolkit Drake.**

***Index Terms*—Simulation and Animation, Contact Modeling, Modeling, Control, and Learning for Soft Robots.**

I. Introduction

ROBOTICS is on the cusp of a new era. Cutting-edge advancements in machine learning, computational power, and manufacturing techniques are pushing the limits of hardware design, sensing, modeling, and control.

The development of soft robotic systems [1], deformable object manipulation capabilities [2], and vision-based tactile sensors [3], [4] has opened up new possibilities for robotics applications. However, these new systems present challenges in modeling and simulation, particularly when the traditional rigid-body assumptions of robotic simulators are no longer valid [2], [5]. Despite these challenges, there is still much potential for growth and innovation in the field of robotics, and the development of open-source simulation capabilities could play a crucial role in advancing the field.

II. Previous Work

Early work in the finite elements community focused on the mathematical formalism and model fidelity of methods for the accurate computation of stresses and deformations at contacting surfaces. Node-on-segment approaches [6], [7] enforce contact such that nodes on a contactor surface do not penetrate their opposing target segments (or facets in three dimensions). Two-pass approaches iterate this process by reversing the role of contactor/target surfaces [8]. However, these methods proved to lack robustness and lead to locking due to over-constraint. To address these problems, the mortar formalism [9] was introduced in segment-to-segment approaches for contact [10], [11].

Manuscript received: March, 2, 2023; Revised June, 1, 2023; Accepted July, 31, 2023.

This paper was recommended for publication by Editor Cecilia Laschi upon evaluation of the Associate Editor and Reviewers' comments.

All authors are with Toyota Research Institute, USA, `firstname.lastname@tri.global`

Digital Object Identifier (DOI): see top of this page.

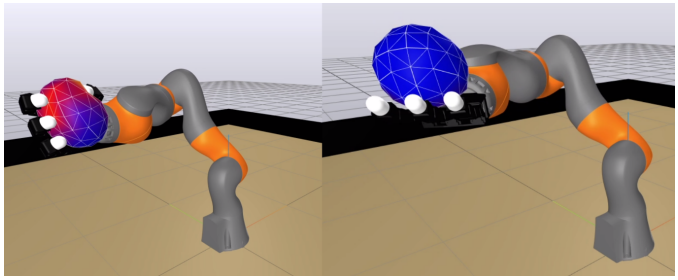

Fig. 1: Simulated robot teleoperated to grasp of a deformable ball (see supplemental video). Contours colored by strain visualize the state of deformations of the ball. Our method resolves the frictional contact between the rigid hand and the deformable ball, enabling a secure grasp at interactive rates.

The computer graphics community has contributed significantly, particularly on performant methods for visually realistic simulations [12]. Projected Gauss Seidel (PGS) and Jacobi variants [13], [14] are popular given they can be easily parallelized. However, they lack robustness due to convergence issues [15]. In the pursuit of increased robustness, optimization based solvers were developed [16], [17], [18]. Work on elements that can recover from inversion [19], [20] and on corotational models [21], [22] further increased the robustness of these formulations at large deformations.

Multibody dynamics with frictional contact is complicated by the non-smooth nature of the solutions. Non-existence of solutions [23], exponential worst-case complexity [24], and NP-hardness [16] have led the community to search alternative formulations. To improve computational tractability, Anitescu introduces a *convex approximation* of the contact problem [25]. For a strictly convex formulation with unique solution, [26] introduces regularization. A convex formulation of compliant contact is presented in [27] and later extended to allow continuous surface patches in [28].

Several open-source software options support deformable object modeling. MuJoCo [29] simulates deformable bodies as a group of connected rigid bodies with spring-dampers. Chrono [30] and Siconos [31] implement the Finite Element Method (FEM), though mostly target large scale applications, such as granular media simulation. Game engines like Bullet [32] and PhysX [33] are popular in reinforcement learning. SOFA [34], initially designed for virtual reality, has also been successful in soft robotics projects.

III. Outline and Novel Contributions

To the knowledge of the authors, this work presents the first convex formulation for the modeling of bodies undergoing large deformations coupled with articulated rigid bodies through frictional contact and holonomic constraints. Despite

IEEE Robotics and Automation Letters (RA-L) paper, presented at ICRA 2024, Yokohama, Japan. Cite as RA-L paper.

IEEE Robotics and Automation Letters (RA-L) paper, presented at ICRA 2024, Yokohama, Japan. Cite as RA-L paper.

the potential for artifacts introduced by the convex approximation of contact, they can be precisely quantified. These effects only become noticeable at high slip velocities, which are usually low in robotic applications [27]. The approximation, however, is extremely powerful, making the problem tractable with strong theoretical guarantees that can be exploited effectively in a practical software implementation [27].

We make a number of novel contributions:

1) **Convex corotational model**. A linear corotational model of large deformations with positive semi-definite Hessian, Section V-B.
2) **Convex formulation of frictional contact**. A convex formulation strongly coupling rigid articulated bodies with deformable objects through frictional contact and holonomic constraints, Section VI.
3) **Schur complement at no additional cost**. We show the expensive-to-compute Schur complement required in the contact problem can be obtained at no additional cost, as an intermediate result in the Cholesky factorization of the momentum equations, Sections VI-A and VI-B.

We present validation and simulation results relevant to robotics in Section VII. Performance metrics show that our method performs well when compared to previous work and this is solely due to the choice of mathematical formulation and algorithms, without resourcing yet to thread-level parallelism. Finally, as part of the open-source robotics toolkit Drake [35], we implement our method with exhaustive testing and thorough documentation.

IV. Mathematical Formulation

The state of our system is described by generalized positions $\mathbf{q} \in \mathbb{R}^{n_q}$ and generalized velocities $\mathbf{v} \in \mathbb{R}^{n_v}$ where n_q and n_v denote the total number of generalized positions and velocities, respectively. Time derivatives of the configurations are related to the generalized velocities by $\dot{\mathbf{q}} = \mathbf{N}(\mathbf{q})\mathbf{v}$, with $\mathbf{N}(\mathbf{q}) \in \mathbb{R}^{n_q \times n_v}$ being the kinematic map. In particular, we use joint coordinates to describe articulated rigid bodies and FEM to spatially discretize deformable bodies. As a result, for deformable bodies, $\mathbf{q}$ and $\mathbf{v}$ are the stacked positions and velocities of the mesh vertices, and the kinematic map $\mathbf{N}$ is the identity.

A. Kinematics of Constraints

We consider n_c constraints described at the velocity level by the constraint velocity $\mathbf{v}_{c,i} \in \mathbb{R}^{r_i}$, with r_i the number of equations for the i-th constraint. For contact constraints, $\mathbf{v}_{c,i}$ corresponds to the relative velocity vector at the i-th contact pair and $r_i = 3$, see [27]. For a holonomic constraint described by $\mathbf{g}_i(\mathbf{q}, t) = 0$, $\mathbf{v}_{c,i} = d\mathbf{g}_i/dt$. We can write constraint velocities in terms of the generalized velocities of the system (including both rigid and deformable body degrees of freedom) as $\mathbf{v}_{c,i} = \mathbf{J}_i\mathbf{v} + \boldsymbol{b}_i$, with $\mathbf{J}_i$ and $\boldsymbol{b}_i = \partial\mathbf{g}_i/\partial t$ the Jacobian and bias, respectively. Collecting all constraints, we define the stacked velocity $\mathbf{v}_c = \mathbf{J}\mathbf{v} + \mathbf{b}$, of size $r = \sum r_i$, where $\mathbf{J}$ and $\mathbf{b}$ are the stacked Jacobian and bias for all constraints.

B. Discrete Time Stepping Scheme

We follow the scheme and notation in [27] closely. We discretize time into intervals of fixed size δt to advance the state of the system from time t_n to the next step at $t_{n+1} = t_n + \delta t$. To simplify notation, we use the naught subscript to denote quantities at t_n while no additional subscript is used for quantities at t_{n+1}. We define quantities evaluated at intermediate time steps $t^\theta = \theta t^{n+1} + (1-\theta)t^n$ in accordance with the standard θ-method using scalar parameters θ and $\theta_{vq} \in [0, 1]$

$$\begin{aligned}\mathbf{q}^\theta &\stackrel{\text{def}}{=} \theta\mathbf{q} + (1-\theta)\mathbf{q}_0,\\ \mathbf{v}^\theta &\stackrel{\text{def}}{=} \theta\mathbf{v} + (1-\theta)\mathbf{v}_0,\\ \mathbf{v}^{\theta_{vq}} &\stackrel{\text{def}}{=} \theta_{vq}\mathbf{v} + (1-\theta_{vq})\mathbf{v}_0,\end{aligned} \tag{1}$$

so that we can accommodate backward Euler with $\theta = \theta_{vq} = 1$, symplectic Euler with $\theta = 0$, $\theta_{vq} = 1$ and the second order midpoint rule with $\theta = \theta_{vq} = 1/2$. Notice that $\theta \neq \theta_{vq}$ for symplectic Euler. Using these definitions we can write the constrained dynamics of rigid and deformable bodies within a unified framework as follows

$$\mathbf{M}(\mathbf{q}^\theta)(\mathbf{v} - \mathbf{v}_0) = \delta t\, \mathbf{k}(\mathbf{q}^\theta, \mathbf{v}^\theta) + \mathbf{J}(\mathbf{q}_0)^T\boldsymbol{\gamma}, \tag{2}$$

$$\mathcal{C} \ni \boldsymbol{\gamma} \perp \mathbf{v}_c - \hat{\mathbf{v}}_c \in \mathcal{C}^*, \tag{3}$$

$$\mathbf{q} = \mathbf{q}_0 + \delta t\mathbf{N}(\mathbf{q}^\theta)\mathbf{v}^{\theta_{vq}}. \tag{4}$$

Equation (2) collects the momentum equations for both rigid and deformable degrees of freedom (DoFs). For each articulated rigid body and deformable body with n_{v_b} DoFs, we use $\mathbf{M}_b$ to denote its mass matrix and $\mathbf{k}_b$ to encode external forces and gyroscopic terms for articulated rigid bodies [27] and internal forces for deformable bodies. We use $\mathbf{M}$ to denote the block diagonal matrix with $\mathbf{M}_b$ as the diagonal blocks and $\mathbf{k}$ to denote the stacked $\mathbf{k}_b$ for all bodies. Rigid and deformable DoFs are coupled through contact and holonomic constraints. Following [36], Eq. (3) encodes both holonomic constraints and the convex approximation of contact constraints. The convex set $\mathcal{C} = \mathcal{C}_1 \times \mathcal{C}_2 \times \cdots \times \mathcal{C}_{n_c}$ is the Cartesian product of sets $\mathcal{C}_i$ for the i-th constraint. For contact constraints, $\mathcal{C}_i$ corresponds to the friction cone $\mathcal{F}_i$ for that contact [27]. For bi-lateral holonomic constraints, $\mathcal{C}_i = \mathbb{R}^{r_i}$ and impulses can take any real value. The *dual* of $\mathcal{C}$ is denoted with $\mathcal{C}^*$. For contact constraints, $\hat{\mathbf{v}}_{c,i}$ encodes information about the contact distance at the previous time step, see [27] for details. For holonomic constraints $\hat{\mathbf{v}}_{c,i} = -\mathbf{g}_i(\mathbf{q}_0)/\delta t$, where $\mathbf{g}_i(\mathbf{q}_0)$ is the constraint error at the previous time step [36]. Finally, Eq. (4) is the positions update in accordance to the θ-method.

Next we discuss modeling of deformable bodies and refer to [27] for details on the treatment of articulated rigid bodies.

V. Modeling Deformable Bodies

Here we describe the equations for a single deformable body and drop the b subscript of $\mathbf{M}$ and $\mathbf{k}$ for simplicity.

A. Preliminaries

We follow a standard formulation of continuum mechanics discretized by FEM. We describe it briefly to provide context

IEEE Robotics and Automation Letters (RA-L) paper, presented at ICRA 2024, Yokohama, Japan. Cite as RA-L paper.

and introduce notation, and refer the reader to [37], [38] for further details. Within this framework, we describe choices specific to our work.

Kinematics is described by the Lagrangian map $\boldsymbol{x} = \boldsymbol{\phi}(\boldsymbol{X}, t)$ from reference positions $\boldsymbol{X}$ to their current position $\boldsymbol{x}$ at time t. We consider hyperelastic solids with an energy density function $\Psi(\mathbf{F}(\boldsymbol{X}))$, with $\mathbf{F} = \partial\boldsymbol{\phi}/\partial\boldsymbol{X}$ the deformation gradient. The elastic potential energy for the solid is

$$E = \int \Psi(\mathbf{F}(\boldsymbol{X}))d\boldsymbol{X},$$

which induces an elastic force $\mathbf{f}_e = -\partial E/\partial\mathbf{q}$. The stiffness matrix is defined as $\mathbf{K} = -\partial\mathbf{f}_e/\partial\mathbf{q}$. Though more sophisticated damping models (e.g. from [39]) may be used, we found the Rayleigh model adequate for our application. The damping force is given by

$$\mathbf{f}_d(\mathbf{v}) = -\left(\alpha\mathbf{M} + \beta\mathbf{K}\right)\mathbf{v}, \tag{5}$$

where α and β are damping coefficients and $\mathbf{M}$ the FEM mass matrix. With these internal forces, $\mathbf{k}$ in Eq. (2) becomes

$$\mathbf{k}(\mathbf{v}) = \mathbf{f}_e(\mathbf{q}^\theta(\mathbf{v})) + \mathbf{f}_d(\mathbf{v}^\theta(\mathbf{v})) + \mathbf{f}_{\text{ext}}, \tag{6}$$

where $\mathbf{f}_{\text{ext}}$ includes constant external forces, such as a gravity.

B. Corotational Material Model

Our framework admits any hyperelastic energy density $\Psi(\mathbf{F}(\boldsymbol{X}))$. We refer readers to [40] for implementation notes and to [41] for a survey of popular choices. However, the stiffness matrix $\mathbf{K}$ can become indefinite and hinder the convergence of iterative solvers [19], [41]. Standard remedies include projecting the energy density Hessian to be positive semi-definite [19] or clamping eigenvalues to be non-negative [42], both associated with additional computational cost. Moreover, linear constitutive models introduce unacceptable artifacts at large rotational deformations [22].

We propose a corotational linear model that enjoys the computational efficiency of the linear model while avoiding rotational artifacts. In particular, we adopt a Saint-Venant-Kirchhoff model with a corotational linear Green strain $\hat{\mathbf{E}}$

$$\Psi(\hat{\mathbf{E}}) = \mu\|\hat{\mathbf{E}}\|_F^2 + \frac{\lambda}{2}\operatorname{tr}(\hat{\mathbf{E}})^2 \tag{7}$$

where μ and λ are Lamé parameters. To define the corotational $\hat{\mathbf{E}}$, we first define a *corotated deformation gradient*

$$\hat{\mathbf{F}}(\boldsymbol{X}) \stackrel{\text{def}}{=} \hat{\mathbf{R}}(\boldsymbol{X})^T\mathbf{F}(\boldsymbol{X})$$

where $\hat{\mathbf{R}}(\boldsymbol{X})$ is a rotation matrix to be chosen to eliminate the rotational component of the deformation. Letting $\mathbf{B} = \hat{\mathbf{F}} - \mathbf{I}$, the Green strain is given by

$$\begin{aligned}\mathbf{E} &= \frac{1}{2}\left(\mathbf{F}^T\mathbf{F} - \mathbf{I}\right)\\ &= \frac{1}{2}\left(\hat{\mathbf{F}}^T\hat{\mathbf{F}} - \mathbf{I}\right) = \frac{1}{2}\left(\left(\mathbf{I} + \mathbf{B}^T\right)\left(\mathbf{I} + \mathbf{B}\right) - \mathbf{I}\right).\end{aligned}$$

By dropping the non-linear term $\mathbf{B}^T\mathbf{B}$, we arrive at the definition of the linearized Green strain

$$\hat{\mathbf{E}} \stackrel{\text{def}}{=} \frac{1}{2}(\hat{\mathbf{F}} + \hat{\mathbf{F}}^T) - \mathbf{I}.$$

With $\hat{\mathbf{R}} = \mathbf{R}$, the rotational component of $\mathbf{F}$ from its polar decomposition, $\hat{\mathbf{E}}$ becomes the strain measure used in [21]. While this eliminates rotational artifacts, the non-linear Ψ can lead to indefiniteness in $\mathbf{K}$. Instead, we approximate $\hat{\mathbf{R}}$ with $\mathbf{R}_0$, the rotational component of the polar decomposition of $\mathbf{F}_0(\boldsymbol{X})$ at the previous time step. With this choice, the energy density is quadratic in $\mathbf{q}$, rotational artifacts are negligible (see results in Section VII), and the stiffness matrix $\mathbf{K}$ is positive semi-definite, as proved in the Appendix. This is equivalent to the method in [22] when the momentum balance is discretized with linear simplex elements and backward Euler, but our formulation naturally generalizes to other time-stepping schemes and non-tetrahedral elements while preserving positive semi-definiteness in $\mathbf{K}$.

VI. Convex Formulation of Constrained Dynamics

From Eq. (2) we define the momentum residual as

$$\mathbf{m}(\mathbf{v}) = \mathbf{M}(\mathbf{q}^\theta(\mathbf{v}))(\mathbf{v} - \mathbf{v}_0) - \delta t\,\mathbf{k}(\mathbf{q}^\theta(\mathbf{v}), \mathbf{v}^\theta(\mathbf{v})). \tag{8}$$

With our corotational model, this is linear in $\mathbf{v}$ for deformable bodies. For rigid bodies, we follow [27] where inertia and damping are treated implicitly for stability and Coriolis and gyroscopic forces are treated explicitly. This allows us to write a linear Eq. (2) as

$$\mathbf{m}(\mathbf{v_0}) + \mathbf{A}(\mathbf{v} - \mathbf{v_0}) = \mathbf{A}(\mathbf{v} - \mathbf{v}^*) = \mathbf{J}^T\boldsymbol{\gamma}, \tag{9}$$

where $\mathbf{A} = \partial\mathbf{m}/\partial\mathbf{v}$ is symmetric positive definite (SPD) and independent of $\mathbf{v}$ and we define

$$\mathbf{v}^* \stackrel{\text{def}}{=} \mathbf{v_0} - \mathbf{A}^{-1}\mathbf{m}(\mathbf{v_0}) \tag{10}$$

as the *free-motion* velocities in the absence of constraints, when $\boldsymbol{\gamma} = \mathbf{0}$ in Eq. (9). Since $\mathbf{A}$ is block diagonal, we solve the free-motion velocities for each body separately. From Section V-A, block $\mathbf{A}_b$ for the b-th deformable body is

$$\mathbf{A}_b = (1 + \alpha\theta\delta t)\,\mathbf{M}_b + \theta\delta t(\theta_{vq}\delta t + \beta)\mathbf{K}_b. \tag{11}$$

We note that this result is exact. Moreover $\mathbf{A}_b$ is SPD since $\mathbf{M}_b$ is SPD and, with our corotational model, $\mathbf{K}_b$ is positive semi-definite. Combining the linear momentum balance (9) with constraints (3) we write a convex formulation as

$$\begin{aligned}&\mathbf{A}(\mathbf{v} - \mathbf{v}^*) = \mathbf{J}^T\boldsymbol{\gamma},\\ &\mathcal{C} \ni \boldsymbol{\gamma} \perp \mathbf{v}_c - \hat{\mathbf{v}}_c \in \mathcal{C}^*.\end{aligned} \tag{12}$$

Equations (12) are the optimality conditions to the following convex optimization problem [36], [27]

$$\begin{aligned}\min_{\mathbf{v}} \quad & \frac{1}{2}\|\mathbf{v} - \mathbf{v}^*\|_A^2\\ \text{s.t.} \quad & \mathbf{J}\mathbf{v} + \mathbf{b} - \hat{\mathbf{v}}_c \in \mathcal{C}^*,\end{aligned} \tag{13}$$

where we used $\mathbf{v}_c = \mathbf{J}\mathbf{v} + \mathbf{b}$ from Section IV-A. To solve Eq. (13), we use the Semi-Analytic Primal (SAP) solver from [27] that formulates a regularized version of this problem with proven global convergence to its unique solution.

A. Participating Degrees of Freedom

SAP [27] solves a non-linear system of equations of size n_v, usually large with deformable bodies in the system. We

IEEE Robotics and Automation Letters (RA-L) paper, presented at ICRA 2024, Yokohama, Japan. Cite as RA-L paper.

exploit the structure of (13) to solve it at interactive rates.

The constraint Jacobian $\mathbf{J}$ for deformable bodies is often sparse because the constraint velocity $\mathbf{v}_{c,i}$ for the i-th constraint only involves a local set of vertices [43]. Moreover, since contact develops at the surface of deformable objects, most columns of $\mathbf{J}$ that correspond to inner mesh vertices are zero. DoFs associated with non-zero columns in $\mathbf{J}$ are herein referred to as *participating* DoFs. All other DoFs are referred to as *non-participating*. For the rest of this section we work on a single body and drop the b-subscript. We use m_p and m_n to denote the number of participating and non-participating DoFs and in general use subscripts p and n for participating and non-participating quantities, respectively. With this partition, we arrange non-participating DoFs to appear first

$$\begin{bmatrix} \mathbf{A}_{nn} & \mathbf{A}_{np} \\ \mathbf{A}_{pn} & \mathbf{A}_{pp} \end{bmatrix} \begin{bmatrix} \boldsymbol{\Delta}\mathbf{v}_n \\ \boldsymbol{\Delta}\mathbf{v}_p \end{bmatrix} = \begin{bmatrix} \mathbf{0} \\ \mathbf{J}_p^T \boldsymbol{\gamma} \end{bmatrix} \tag{14}$$

with $\boldsymbol{\Delta}\mathbf{v} \overset{\text{def}}{=} \mathbf{v} - \mathbf{v}^*$ and $\mathbf{J}_p$ being the columns of $\mathbf{J}$ corresponding to participating DoFs of the deformable body under consideration. This partition leads to an (often large) block of zeros of size m_n on the right-hand side. This allows us to eliminate $\boldsymbol{\Delta}\mathbf{v}_n$ algebraically

$$\boldsymbol{\Delta}\mathbf{v}_n = -\mathbf{A}_{nn}^{-1}\mathbf{A}_{np}\boldsymbol{\Delta}\mathbf{v}_p \tag{15}$$

to obtain a system in terms of participating DoFs only

$$\hat{\mathbf{A}}\boldsymbol{\Delta}\mathbf{v}_p = \mathbf{J}_p^T\boldsymbol{\gamma} \tag{16}$$

where $\hat{\mathbf{A}} = \mathbf{A}_{pp} - \mathbf{A}_{pn}\mathbf{A}_{nn}^{-1}\mathbf{A}_{np} \in \mathbb{R}^{m_p \times m_p}$ is the Schur complement of $\mathbf{A}$. Since constraints in (13) only involve participating DoFs, we can now solve a much smaller optimization problem in terms of participating DoFs

$$\begin{aligned} \min_{\mathbf{v}} \quad & \frac{1}{2}\|\mathbf{v} - \mathbf{v}_p^*\|_{\hat{A}}^2 \\ \text{s.t.} \quad & \mathbf{J}\mathbf{v} + \mathbf{b} - \hat{\mathbf{v}}_c \in \mathcal{C}^*, \end{aligned} \tag{17}$$

with $\mathbf{v}_p^*$ corresponding to participating DoFs only. We then use (15) to update non-participating DoFs velocities.

B. Schur Complement Computation

Forming $\mathbf{A}_{nn}^{-1}$ needed in the Schur complement $\hat{\mathbf{A}}$ is computationally expensive and impractical. However, we can obtain $\hat{\mathbf{A}}$ at no additional cost during the factorization of $\mathbf{A}$ for the computation of free-motion velocities in Eq. (10). We start from the factorization of the permuted $\mathbf{A}$

$$\begin{bmatrix} \mathbf{A}_{nn} & \mathbf{A}_{np} \\ \mathbf{A}_{pn} & \mathbf{A}_{pp} \end{bmatrix} = \begin{bmatrix} \mathbf{L}_{nn} & \mathbf{0} \\ \mathbf{L}_{pn} & \mathbf{L}_{pp} \end{bmatrix} \begin{bmatrix} \mathbf{L}_{nn} & \mathbf{0} \\ \mathbf{L}_{pn} & \mathbf{L}_{pp} \end{bmatrix}^T \tag{18}$$

to see that

$$\begin{aligned} \hat{\mathbf{A}} =& \ \mathbf{A}_{pp} - \mathbf{A}_{pn}\mathbf{A}_{nn}^{-1}\mathbf{A}_{pp} \\ =& \ \mathbf{L}_{pn}\mathbf{L}_{pn}^T + \mathbf{L}_{pp}\mathbf{L}_{pp}^T - \mathbf{L}_{pn}\mathbf{L}_{nn}^T(\mathbf{L}_{nn}\mathbf{L}_{nn}^T)^{-1}\mathbf{L}_{nn}\mathbf{L}_{pn}^T \\ =& \ \mathbf{L}_{pp}\mathbf{L}_{pp}^T \\ =& \ \mathbf{A}_{pp} - \mathbf{L}_{pn}\mathbf{L}_{pn}^T, \end{aligned}$$

We then factorize $\mathbf{A}$ using a right-looking Cholesky factorization and record the Schur complement $\hat{\mathbf{A}}$ after block $\mathbf{A}_{nn}$ is factorized. Moreover, the same factorization of $\mathbf{A}$ is used to solve (10) and (15). Equations within participating and non-participating partitions can be reordered to reduce fill-ins in the factorization. We observe that AMD ordering [44] within a partition leads to fewer fill-ins than arbitrary ordering.

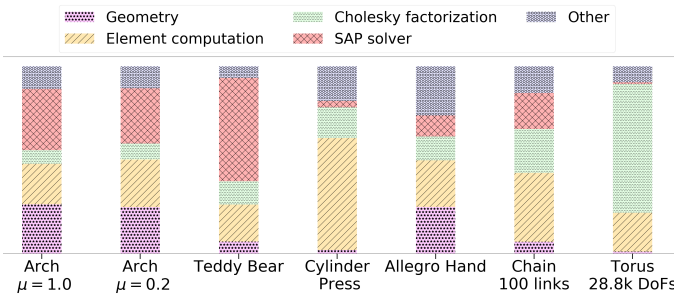

Fig. 2: Total runtime split among main computations.

VII. Results and Discussion

We present test cases to assess the robustness, accuracy, and performance of our method. All simulations are carried out in a system with two 16-core Intel® Xeon® Gold 6226R Processors and 192 GB of RAM, running Ubuntu 20.04. However, all of our tests are run in a single thread. We report scene statistics and performance in Table I and timing breakdowns of the most time-consuming routines in Fig. 2. We observe that geometry and the element-wise FEM computations are embarrassingly parallelizable and can immediately benefit from a parallel implementation. On the other hand, computations for the SAP solver and the Cholesky factorization for Eq. (14) are less amenable to parallelization and require careful investigation. The SAP problem for the masonry arch and chain examples essentially is block tridiagonal, and SAP's supernodal solver [45] can effectively exploit this structure. However, the structure of the problem is very close to dense for the teddy bear example, and SAP factorizations become the bottleneck. In addition, in less dynamic scenes (e.g. the masonry arch and the cylinder press), SAP benefits from its warm-start strategy [27]. Scalability of SAP with the number of bodies is studied in [27] and with the number of constraints in [28]. All examples use our corotational model except for the cylinder press benchmark, which uses a model to match published results. Unless otherwise specified, the Rayleigh damping model uses $\alpha = 0$ and $\beta = 0.01$. For all simulation results, SAP runs to convergence with relative tolerance $\varepsilon_r = 10^{-6}$ [27].

A. Rubber Cylinder Pressed Between Two Rigid Plates

We validate contact resolution and internal stresses against a benchmark extensively studied in the engineering literature, with well-known numerical solution [46], [47], [48].

A homogeneous cylinder 0.4 meter in diameter is pressed between two frictionless rigid plates, Fig. 3. The material of the cylinder is modeled as Mooney-Rivlin rubber with constants $C_1 = 0.293$ MPa, $C_2 = 0.177$ MPa, and bulk modulus 1410 MPa. In particular, we use the formulation in [41] for its rest stability. Density is 1000 kg/m^3 and there is no gravity. As in previous literature, we consider a plane state of strains. To achieve that in our inherently 3D formulation,

IEEE Robotics and Automation Letters (RA-L) paper, presented at ICRA 2024, Yokohama, Japan. Cite as RA-L paper.

TABLE I: Timing and scene statistics. We account for rigid and deformable DoFs, with 3 DoFs per mesh vertex. The realtime rate is the ratio of simulated time over CPU time.

Example	DoFs	Time Step (sec)	Realtime Rate	Constraints Average (Max)
Arch ($\mu = 0.2$)	225	0.04	7.26	259.5 (357)
Arch ($\mu = 1.0$)	225	0.04	6.29	320.2 (364)
Cylinder press	3796	0.01	0.06	248.3 (335)
Allegro hand	410	0.01	1.13	380.7 (863)
Teddy bear	2043	0.02	0.37	236.5 (464)
Chain with 100 links	90000	0.02	0.020	3880.2 (5663)
Single torus	28800	0.02	0.017	53.0 (394)

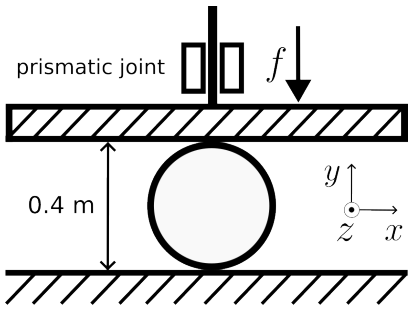

Fig. 3: Rubber cylinder pressed between rigid plates.

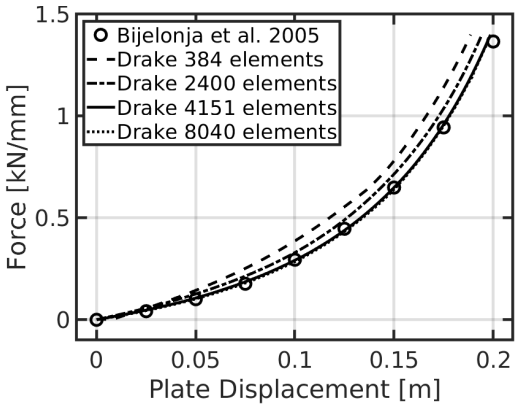

Fig. 4: Force-displacement curve for the cylinder press, Fig. 3. Convergence is attained under mesh refinement.

we mesh the cylinder with two layers of linear tetrahedral elements along the z-direction, assume $\partial/\partial z = 0$ in the computation of the deformation gradient $\boldsymbol{F}$, and impose zero out of plane displacements to avoid drift due to round-off errors. We apply a downward force on the top plate through a prismatic joint and measure the resulting displacement. As the top plate is pressed downward, contact constraints are resolved automatically by our method. We increase the magnitude of the force linearly in time from zero to $f_{\text{max}} = 1.4$ MN/m, to match [46]. To better compare with static analysis results in the literature, we reduce inertial effects by overdamping the cylinder with $\beta = 0.5$ and by slowly applying the load over a period of 500 seconds. We perform a mesh refinement study using four progressively finer meshes. The force-displacement curves obtained with our method are shown in Fig. 4 along with the reference solution from [46]. As the spatial resolution is increased, the force-displacement curves converge to the reference solution.

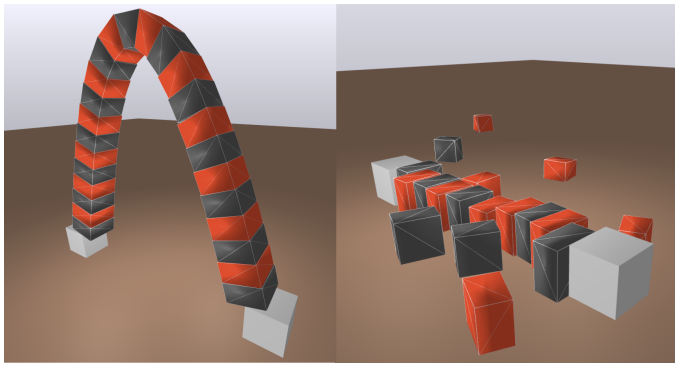

Fig. 5: Masonry arch. Each block is modeled as a stiff deformable object to stress test stability and showcase contact among deformable bodies. With $\mu = 1.0$, the structure stable (left) whereas with $\mu = 0.2$, the structure falls apart (right).

B. Masonry Arch

We test the robustness of our method on the frictionally dependent stable arch tests from [16], [18], [49]. In particular, we take the additionally challenging setup from [18] where the arch has its base balanced on sharp edges. Similar to [18], we simulate very stiff blocks in the arch with a high Young's modulus of 20 GPa, Poisson's ratio 0.3, and density 2300 kg/m^3. While stiff non-linear models often struggle to converge due to ill-conditioning, our corotated model leads to a linear free-motion equation (10) that is solved to machine precision. Our method resolves the frictional contacts among the blocks stably at 40 ms time step. We simulate the structure for 10 minutes and verify the blocks with friction coefficient $\mu = 1.0$ form a long-term stable arch. We also confirm that the structure falls apart with a lower friction coefficient $\mu = 0.2$. Our method has guaranteed convergence and therefore simulation results always satisfy momentum balance, the model of Coulomb friction, and the maximum dissipation principle.

C. Soft-bubble Gripper

We simulate a *Soft-bubble* gripper [3] manipulating a deformable teddy bear, Fig. 6. This is a Schunk WSG 50 gripper with air filled rubber chambers providing highly compliant gripping surfaces. We model the air-inflated chambers as deformable volumetric objects with Young's modulus 50 kPa and Poisson's ratio 0.3. The flat base of the bubbles are attached to the gripper fingers using holonomic constraints. The teddy bear is modeled with Young's modulus 10 kPa

IEEE Robotics and Automation Letters (RA-L) paper, presented at ICRA 2024, Yokohama, Japan. Cite as RA-L paper.

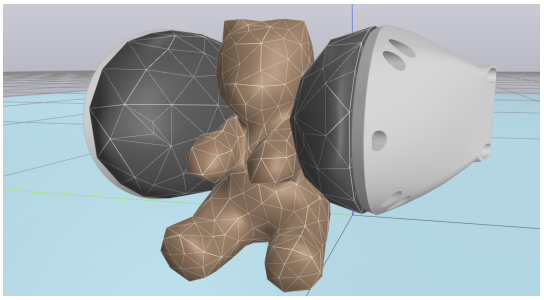

Fig. 6: Highly compliant *Soft-bubble* gripper [3] securing the grasp of a deformable teddy bear.

and Poisson's ratio 0.4. The gripper is PD-controlled with a prescribed *close-lift-shake-place* motion sequence. We perform the shaking motion to stress test the stability of the grasp in simulation, see the supplemental video. The entire system with 2043 DoFs is highly coupled via up to 464 constraints. Our solver is able to solve all time steps of this challenging scenario to convergence.

D. Interactive Control

A KUKA LBR iiwa arm (7 DoFs) outfitted with an anthropomorphic Allegro hand (16 DoFs) is teleoperated to manipulate a deformable ball, Fig. 1. Though we added the arm, this case is inspired by the example in [49]. A differential inverse kinematics controller computes desired states given an end effector pose controlled interactively with a gamepad. The deformable ball is modeled with Young's modulus 25 kPa and Poisson's ratio 0.4. As the robot closes its palm around the ball, contact patches between the ball and the palm, phalanges, and fingertips of the hand establish a secure grasp. We apply a shaking motion to stress test the stability of the grasp, see supplemental video. Even with the overhead of the controller, our simulation runs at real-time rates.

E. Cantilever Beam

To assess the quality of the approximation $\hat{\mathbf{R}} = \mathbf{R}_0$ in Section V-B, we study the effect of time step size in the large deformations of a cantilever beam subject to gravity, Fig. 7. The white beam is modeled with our proposed corotational linear model while the red beam is modeled using the traditional corotational model from [21]. With a very large one second time step, our model shows spurious volume gains described in [22] given the approximation $\hat{\mathbf{R}} \approx \mathbf{R}_0$, though it remains stable. In contrast, simulations with the traditional corotational model become unstable. As we refine time steps, the solutions of the two models converge.

F. Scalability Analysis

We simulate a chain of deformable links hung from a fixed (white) torus under gravity, Fig. 8. Each link has 300 vertices, 720 tetrahedra, density $500\ \mathrm{kg/m^3}$, Young's modulus 10 MPa and Poisson's ratio 0.4. The setup closely resembles the comparison in [18] with the open-source simulation framework SOFA [34]. To verify the chain structure sustains, we run 60 seconds of simulated time. Figure 8 shows wall-clock time

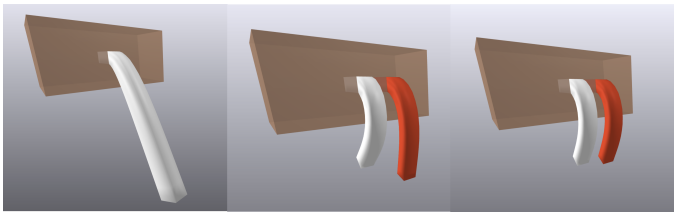

Fig. 7: Comparison between our proposed corotational linear model (white) and the corotational model from [21] (red). The time step size from left to right are 1s, 100ms, and 10ms. The state at time 1s is shown.

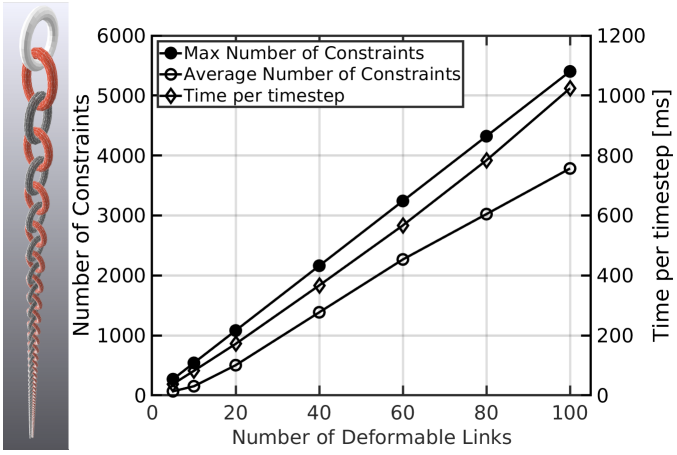

Fig. 8: Steady state for a chain of 100 deformable links under gravity. Wall-clock per time step, maximum and average number of constraints vs. problem size.

and number of constraints as we increase the number of links in the chain, totaling up to 90k DoFs and 5.6k constraints. Given the sparse structure of the contact problem, the runtime scales linearly with the problem size.

We also study scalability in a mesh refinement study. We keep one deformable link from the previous experiment and vary its mesh resolution. Figure 9 illustrates the setup of the experiment and timing statistics. The runtime scales superlinearly with the number of DoFs due to the Cholesky factorization of $\mathbf{A}$.

For both studies we use 20 ms time steps and $\beta = 0.05$.

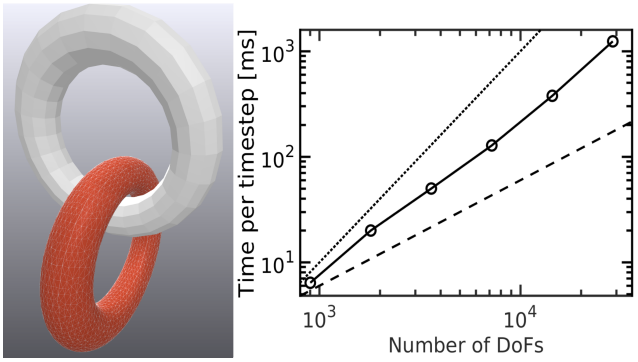

Fig. 9: Deformable torus with 28.8k DoFs hung from a fixed rigid torus. Wall-clock vs. DoFs. Linear (dashed) and quadratic (dotted) scaling are shown for reference.

IEEE Robotics and Automation Letters (RA-L) paper, presented at ICRA 2024, Yokohama, Japan. Cite as RA-L paper.

VIII. Limitations and Future Work

We summarize the limitations we have identified for our method and propose future research directions.

Parallel implementation: With a focus on accuracy and algorithms, our implementation for this work is serial. Some of the most time-consuming computations can easily benefit from a parallel implementation, while the same is not obvious for the SAP solver and the Cholesky factorization computation. Leveraging the power of parallelization on modern hardware is an interesting area for future investigation.

Rotational invariance: As with all other linear constitutive models, our linearized model with lagged rotational component is not rotationally invariant. Thus it is not suitable to simulate fast rotational deformations at large time steps. This drawback, however, only manifests itself in the presence of extremely large time steps as we demonstrate in Section VII-E which is uncommon for robotics applications. We have not observed instability from lagging the rotation. In the supplemental video, we show that the cantilever beam from Section VII-E remains stable under extreme deformation.

Self-contact: We do not consider self-contact at the moment due to the lack of support by our geometry engine. Self-contact can be incorporated into our method by updating the geometry engine to augment the set of contacts reported.

Tunneling at high speeds: Though our method has a lower computational cost, it could benefit from continuous collision detection strategies [18] to provide constraints before contact is established. This would allow to mitigate issues such as objects tunneling past each other at high speeds. Efficient solutions to mitigate this issue is a topic of active research for the authors.

Redundant constraints: Even though our SAP solver [27] provides existence and uniqueness guarantees, a large number of constraints hurts performance as can be observed in the *Soft-bubble* example. We currently investigate strategies to handle large number of constraints without sacrificing accuracy.

Convex approximation artifacts: Artifacts introduced by the convex approximation of contact are well identified in [27]. These can only become apparent at high slip velocities, uncommon in robotic applications.

IX. Conclusions

We present what we believe is the first convex formulation of bodies undergoing large deformations coupled with articulated rigid bodies through contact and holonomic constraints.

To achieve this, we introduce a material model in terms of a linearized Green strain and demonstrate that our formulation is linear with a positive semi-definite stiffness matrix when the rotational component of the deformation gradients is lagged. This allows us to incorporate the modeling of large deformations into our previous convex formulation of contact [27]. We exploit the structure of the problem in two ways. Firstly, we partition the problem and express it as a smaller optimization program that only includes constrained variables. Secondly, we show how the expensive-to-compute Schur complements required in the optimization problem can be obtained at no additional cost as an intermediate computation in the Cholesky factorization of the momentum balance equations.

We present validation results and simulations relevant to robotics. Specifically, we showcase our approach to resolve stable grasps in two challenging manipulation tasks robustly.

Profiling reveals that parallelization of geometry and FEM elemental routines is attractive in cases with a much larger number of DoFs than constraints. However, cases dominated by the number of constraints are less amenable to parallelization since they are dominated by the cost of factorizations and the SAP solver. Our analysis includes a summary of limitations and future research directions. Even though our results show performance on par with existing approaches and sometimes even better, the main gain from our method is robustness. Unlike other approaches that run a fixed number of iterations to stay within a specified computational budget, our method always solves the problem to convergence at real-time rates. This is enabled by the strong convergence guarantees of our SAP solver [27]. Therefore, simulation results always satisfy the momentum equations and friction laws without introducing difficult-to-detect artifacts. This aspect is particularly critical for the meaningful sim-to-real transfer of results.

Finally, we incorporated our method into the open-source robotics toolkit Drake [35] and hope that the simulation and robotics communities can benefit from our contribution.

Appendix

Proposition 1. *The constitutive model defined in Eq.* (7) *is quadratic in* $\mathbf{q}$ *and the resulting stiffness matrix* $\mathbf{K}$ *is positive semi-definite.*

Proof. Recall that $\hat{\mathbf{E}} = \frac{1}{2}(\hat{\mathbf{R}}^T\mathbf{F} + \mathbf{F}^T\hat{\mathbf{R}}) - \mathbf{I}$ for some constant $\hat{\mathbf{R}}$ and thus $\hat{\mathbf{E}}$ is linear in $\mathbf{F}$ which in turn is linear in $\mathbf{q}$. Therefore, it suffices to show that $\Psi(\hat{\mathbf{E}})$ is quadratic in $\hat{\mathbf{E}}$ and its Hessian is positive semi-definite. Indeed, differentiating Ψ with respect to $\hat{\mathbf{E}}$ twice gives

$$\frac{\partial^2 \Psi}{\partial \hat{\mathbf{E}}^2} = 2\mu\mathcal{I} + \lambda \mathbf{I} \otimes \mathbf{I},$$

where $\mathcal{I}$ and $\mathbf{I}$ denote unit fourth and second order tensors respectively. Since this Hessian is constant Ψ is quadratic in $\hat{\mathbf{E}}$. For an arbitrary second order tensor $\mathbf{dE}$, we have

$$\mathbf{dE} : \frac{\partial^2 \Psi}{\partial \hat{\mathbf{E}}^2} : \mathbf{dE} = 2\mu \|\mathbf{dE}\|_F^2 + \lambda \operatorname{tr}(\mathbf{dE})^2 \geq 0,$$

and therefore $\partial^2\Psi/\partial\hat{\mathbf{E}}^2$ is positive definite and consequently $\mathbf{K}$ is positive semi-definite. □

Acknowledgment

We are grateful for the continuous patience and support from Dynamics & Simulation and Dexterous Manipulation teams at TRI. We thank Frank Permenter for helpful discussions and Damrong Guoy for geometry support.

References

[1] F. Schmitt, O. Piccin, L. Barbé, and B. Bayle, "Soft robots manufacturing: A review," *Frontiers in Robotics and AI*, vol. 5, p. 84, 2018.

[2] J. Zhu, A. Cherubini, C. Dune, D. Navarro-Alarcon, F. Alambeigi, D. Berenson, F. Ficuciello, K. Harada, J. Kober, X. Li, *et al.*, "Challenges and outlook in robotic manipulation of deformable objects," *IEEE Robotics & Automation Magazine*, vol. 29, no. 3, pp. 67–77, 2022.

[3] N. Kuppuswamy, A. Alspach, A. Uttamchandani, S. Creasey, T. Ikeda, and R. Tedrake, "Soft-bubble grippers for robust and perceptive manipulation," in *2020 IEEE/RSJ International Conference on Intelligent Robots and Systems (IROS)*. IEEE, 2020, pp. 9917–9924.

[4] A. Agarwal, T. Man, and W. Yuan, "Simulation of vision-based tactile sensors using physics based rendering," in *2021 IEEE International Conference on Robotics and Automation (ICRA)*. IEEE, 2021, pp. 1–7.

[5] X. Lin, Y. Wang, J. Olkin, and D. Held, "Softgym: Benchmarking deep reinforcement learning for deformable object manipulation," in *Conference on Robot Learning*. PMLR, 2021, pp. 432–448.

[6] J. Hallquist, G. Goudreau, and D. Benson, "Sliding interfaces with contact-impact in large-scale lagrangian computations," *Computer methods in applied mechanics and engineering*, vol. 51, no. 1-3, pp. 107–137, 1985.

[7] A. B. Chaudhary and K.-J. Bathe, "A solution method for static and dynamic analysis of three-dimensional contact problems with friction," *Computers & Structures*, vol. 24, no. 6, pp. 855–873, 1986.

[8] E. Bittencourt and G. J. Creus, "Finite element analysis of three-dimensional contact and impact in large deformation problems," *Computers & structures*, vol. 69, no. 2, pp. 219–234, 1998.

[9] Y. Maday, C. Mavriplis, and A. Patera, "Nonconforming mortar element methods: application to spectral discretizations," NASA CR 181729, ICASE-88-59, Tech. Rep., 1988.

[10] T. McDevitt and T. Laursen, "A mortar-finite element formulation for frictional contact problems," *International Journal for Numerical Methods in Engineering*, vol. 48, no. 10, pp. 1525–1547, 2000.

[11] M. A. Puso and T. A. Laursen, "A mortar segment-to-segment frictional contact method for large deformations," *Computer methods in applied mechanics and engineering*, vol. 193, no. 45-47, pp. 4891–4913, 2004.

[12] S. Andrews, K. Erleben, and Z. Ferguson, "Contact and friction simulation for computer graphics," in *ACM SIGGRAPH 2022 Courses*, 2022, pp. 1–172.

[13] M. Müller, B. Heidelberger, M. Hennix, and J. Ratcliff, "Position based dynamics," *Journal of Visual Communication and Image Representation*, vol. 18, no. 2, pp. 109–118, 2007.

[14] T. Shinar, C. Schroeder, and R. Fedkiw, "Two-way coupling of rigid and deformable bodies," in *Proceedings of the 2008 ACM SIGGRAPH/Eurographics Symposium on Computer Animation*, 2008, pp. 95–103.

[15] K. Erleben, "Velocity-based shock propagation for multibody dynamics animation," *ACM Transactions on Graphics (TOG)*, vol. 26, no. 2, pp. 12–es, 2007.

[16] D. M. Kaufman, S. Sueda, D. L. James, and D. K. Pai, "Staggered projections for frictional contact in multibody systems," *ACM Trans. Graph.*, vol. 27, no. 5, Dec. 2008.

[17] M. Macklin, K. Erleben, M. Müller, N. Chentanez, S. Jeschke, and T.-Y. Kim, "Primal/dual descent methods for dynamics," in *Computer Graphics Forum*, vol. 39, no. 8. Wiley Online Library, 2020, pp. 89–100.

[18] M. Li, Z. Ferguson, T. Schneider, T. Langlois, D. Zorin, D. Panozzo, C. Jiang, and D. M. Kaufman, "Incremental potential contact: Intersection- and inversion-free large deformation dynamics," *ACM Trans. Graph. (SIGGRAPH)*, vol. 39, no. 4, 2020.

[19] J. Teran, E. Sifakis, G. Irving, and R. Fedkiw, "Robust quasistatic finite elements and flesh simulation," in *Proceedings of the 2005 ACM SIGGRAPH/Eurographics symposium on Computer animation*, 2005, pp. 181–190.

[20] A. Stomakhin, R. Howes, C. A. Schroeder, and J. M. Teran, "Energetically consistent invertible elasticity." in *Symposium on Computer Animation*, vol. 1, no. 2, 2012.

[21] A. McAdams, Y. Zhu, A. Selle, M. Empey, R. Tamstorf, J. Teran, and E. Sifakis, "Efficient elasticity for character skinning with contact and collisions," in *ACM SIGGRAPH 2011 papers*, 2011, pp. 1–12.

[22] M. Müller and M. H. Gross, "Interactive virtual materials." in *Graphics interface*, vol. 2004, 2004, pp. 239–246.

[23] D. Baraff, "Issues in computing contact forces for non-penetrating rigid bodies," *Algorithmica*, vol. 10, no. 2, pp. 292–352, 1993.

[24] ——, "Fast contact force computation for nonpenetrating rigid bodies," in *Proceedings of the 21st annual conference on Computer graphics and interactive techniques*, 1994, pp. 23–34.

[25] M. Anitescu, "Optimization-based simulation of nonsmooth rigid multibody dynamics," *Mathematical Programming*, vol. 105, no. 1, pp. 113–143, 2006.

[26] E. Todorov, "Convex and analytically-invertible dynamics with contacts and constraints: Theory and implementation in mujoco," in *2014 IEEE International Conference on Robotics and Automation (ICRA)*. IEEE, 2014, pp. 6054–6061.

[27] A. M. Castro, F. N. Permenter, and X. Han, "An unconstrained convex formulation of compliant contact," *IEEE Transactions on Robotics*, 2022.

[28] J. Masterjohn, D. Guoy, J. Shepherd, and A. Castro, "Velocity level approximation of pressure field contact patches," *IEEE Robotics and Automation Letters*, vol. 7, no. 4, pp. 11 593–11 600, 2022.

[29] E. Todorov, T. Erez, and Y. Tassa, "Mujoco: A physics engine for model-based control," in *2012 IEEE/RSJ International Conference on Intelligent Robots and Systems*. IEEE, 2012, pp. 5026–5033.

[30] A. Tasora, R. Serban, H. Mazhar, A. Pazouki, D. Melanz, J. Fleischmann, M. Taylor, H. Sugiyama, and D. Negrut, "Chrono: An open source multi-physics dynamics engine," T. Kozubek, Ed. Springer, 2016, pp. 19–49.

[31] V. Acary, O. Bonnefon, M. Brémond, O. Huber, F. Pérignon, and S. Sinclair, "An introduction to siconos," INRIA, Tech. Rep., 2019.

[32] E. Coumans and Y. Bai, "Pybullet, a python module for physics simulation for games, robotics and machine learning," http://pybullet.org, 2016–2020.

[33] "NVIDIA PhysX," https://github.com/NVIDIA-Omniverse/PhysX, accessed: 2023-02-27.

[34] F. Faure, C. Duriez, H. Delingette, J. Allard, B. Gilles, S. Marchesseau, H. Talbot, H. Courtecuisse, G. Bousquet, I. Peterlik, and S. Cotin, "SOFA: A Multi-Model Framework for Interactive Physical Simulation," in *Soft Tissue Biomechanical Modeling for Computer Assisted Surgery*, ser. Studies in Mechanobiology, Tissue Engineering and Biomaterials, Y. Payan, Ed. Springer, June 2012, vol. 11, pp. 283–321. [Online]. Available: https://hal.inria.fr/hal-00681539

[35] R. Tedrake and the Drake Development Team, "Drake: Model-based design and verification for robotics," https://drake.mit.edu, 2019.

[36] H. Mazhar, D. Melanz, M. Ferris, and D. Negrut, "An analysis of several methods for handling hard-sphere frictional contact in rigid multibody dynamics," Citeseer, Tech. Rep., 2014.

[37] J. Bonet, A. J. Gil, and R. D. Wood, *Nonlinear solid mechanics for finite element analysis: dynamics*. Cambridge University Press, 2021.

[38] T. Belytschko, W. K. Liu, B. Moran, and K. Elkhodary, *Nonlinear finite elements for continua and structures*. John wiley & sons, 2014.

[39] R. M. Sánchez-Banderas and M. A. Otaduy, "Strain rate dissipation for elastic deformations," in *Computer Graphics Forum*, vol. 37, no. 8. Wiley Online Library, 2018, pp. 161–170.

[40] E. Sifakis and J. Barbic, "FEM simulation of 3d deformable solids: a practitioner's guide to theory, discretization and model reduction," in *Acm siggraph 2012 courses*, 2012, pp. 1–50.

[41] T. Kim and D. Eberle, "Dynamic deformables: implementation and production practicalities," in *ACM SIGGRAPH 2020 Courses*, 2020, pp. 1–182.

[42] B. Smith, F. D. Goes, and T. Kim, "Analytic eigensystems for isotropic distortion energies," *ACM Transactions on Graphics (TOG)*, vol. 38, no. 1, pp. 1–15, 2019.

[43] Z. Zeng, S. Cotin, and H. Courtecuisse, "Real-time fe simulation for large-scale problems using precondition-based contact resolution and isolated dofs constraints," in *Computer Graphics Forum*, vol. 41, no. 6. Wiley Online Library, 2022, pp. 418–434.

[44] P. R. Amestoy, T. A. Davis, and I. S. Duff, "An approximate minimum degree ordering algorithm," *SIAM Journal on Matrix Analysis and Applications*, vol. 17, no. 4, pp. 886–905, 1996.

[45] T. A. Davis, S. Rajamanickam, and W. M. Sid-Lakhdar, "A survey of direct methods for sparse linear systems," *Acta Numerica*, vol. 25, pp. 383–566, 2016.

[46] I. Bijelonja, I. Demirdžić, and S. Muzaferija, "A finite volume method for large strain analysis of incompressible hyperelastic materials," *International journal for numerical methods in engineering*, vol. 64, no. 12, pp. 1594–1609, 2005.

[47] T. Sussman and K.-J. Bathe, "A finite element formulation for nonlinear incompressible elastic and inelastic analysis," *Computers & Structures*, vol. 26, no. 1-2, pp. 357–409, 1987.

[48] A. M. A. V. Manual, "Vm201: Rubber cylinder pressed between two plates," *ANSYS, Inc. Release*, vol. 15, pp. 539–542, 2013.

[49] M. Macklin, K. Erleben, M. Müller, N. Chentanez, S. Jeschke, and V. Makoviychuk, "Non-smooth newton methods for deformable multi-body dynamics," *ACM Transactions on Graphics (TOG)*, vol. 38, no. 5, pp. 1–20, 2019.

IEEE Robotics and Automation Letters (RA-L) paper, presented at ICRA 2024, Yokohama, Japan. Cite as RA-L paper.